Supplemental Material

C_H2 Domain Orientation of Human Immunoglobulin G in Solution: Structural Comparison of Glycosylated and Aglycosylated Fc Regions Using Small-Angle X-Ray Scattering

Seiki Yageta,[†,‡,§] Hiroshi Imamura,[¶,‡] Risa Shibuya[†] and Shinya Honda[†,‡,§]

[†]Department of Computational Biology and Medical Sciences, Graduate School of Frontier Sciences, the University of Tokyo, 5-1-5 Kashiwanoha, Kashiwa, Chiba 277-8562, Japan

[‡]Biomedical Research Institute, National Institute of Advanced Industrial Science and Technology, AIST Central 6, 1-1-1 Higashi, Tsukuba, Ibaraki 305-8566, Japan

[§]Manufacturing Technology Association of Biologics, Tsukuba Center Inc., 1-1-1 Sengen, Tsukuba, Ibaraki 305-0047, Japan

[¶]Department of Applied Chemistry, College of Life Sciences, Ritsumeikan University, 1-1-1 Nojihigashi, Kusatsu, Shiga 525-8577, Japan

Correspondence to Shinya Honda: s.honda@aist.go.jp

This file includes

SUPPLEMENTARY METHOD

SAXS Data Processing

Raw scattering intensities of the buffer solutions were subtracted from those of protein solutions, and converted to an absolute scattering intensity, $I(q)$ (cm^{-1}), using the zero-angle scattering intensity of water as a standard.[1, 2] Accordingly, q is the scattering parameter and the magnitude of the scattering vector (**q**), given by:

$$q = |\mathbf{q}| = 4\pi \sin\theta/\lambda$$

where 2θ is the scattering angle and λ is the wavelength of the X-ray.[3]

Interference-free SAXS profiles were calculated as follows.[4] First, the normalization of the measured SAXS profiles [$cm^{-1}(mg/mL)^{-1}$] was performed by multiplying the scaling factor[5] between the measured SAXS profiles of 2 to 5 mg/mL protein concentrations and their averaged SAXS profiles calculated in the q region from 0.03 to 0.1 $Å^{-1}$. Then, the small q region from 0.005 to 0.05 $Å^{-1}$ of the interference-free SAXS profile was estimated by extrapolating the normalized SAXS profiles to infinite dilution. The large q region from 0.05 to 0.35 $Å^{-1}$ of the interference-free SAXS profiles was calculated using the averaged SAXS profile.

The radius of gyration (R_g) and the scattering intensity at zero-angle [$I(0)$] were determined by the Guinier approximation (to satisfy $qR_g < 1.3$) in the Guinier region ($0 < q < 1/R_g$) of the scattering profiles, as follows:[3]

$$I(q) \approx I(0) \exp\left(-\frac{R_g^2 q^2}{3}\right)$$

The relationship between the estimated molecular mass (M) of samples and $I(0)$ is as follows:

$$M = \frac{I(0) N_A}{c\left(\bar{v}_p \Delta\rho_p\right)^2}$$

where N_A is the Avogadro's number; c is the protein concentration (g cm^{-3}); $\bar{v}_p$ is the partial specific volume of the protein (here, 0.7425 cm^3 g^{-1})[6]; and $\Delta\rho_p$ is the average excess scattering density of the protein (2.8×10^{10} cm^{-2}).[6]

Before calculating the pair-distance distribution function, $P(r)$, the measured SAXS profiles [cm^{-1}] were normalized by dividing them by the molar concentration [mol/L] of samples, meaning that the SAXS profiles were normalized based on the number of particles. Then, $P(r)$ was calculated by a

direct Fourier transformation of $I(q)$, according to the following equation:[7-10]

$$P(r) = \frac{1}{2\pi^2}\int_0^\infty I(q)qr\sin(qr)\exp(-Bq^2)\,\mathrm{d}q$$

where r is the distance between electrons in the particle; and B (here, 20) is the damping factor to remove the termination effect of the Fourier transformation. An indirect Fourier transformation was also performed using the GNOM program.[11] The maximum distance of the particle (D_{max}), where $P(r)$ approaches zero, was estimated from $P(r)$.

SUPPLEMENTARY DISCUSSION

The Proof for $R_{g\ hollow} > R_{g\ rigid}$

The *N*-linked glycan of gFc is located near the center of the three-dimensional structure of Fc, filling the hollow between the two C_H2 domains. When the gFc and aFc structures are modeled as rigid and hollow spheres, respectively, the effect of the scattering from the *N*-linked glycan on R_g may be derived. In this case, R_g of a rigid or hollow sphere is expressed as,[12]

$$R_g^2 = \frac{\int_V \rho(r)\, r^2 dV}{\int_V \rho(r)\, dV} = \frac{\int_{r_1}^{r_2} \rho(r) r^4 dr}{\int_{r_1}^{r_2} \rho(r) r^2 dr}$$

where $\rho(r)$ is the scattering density of a sample, which can be considered constant in this system; r is the distance between an electron and the center of the rigid or hollow sphere; r_1 and r_2 are the distances from the center to the inner and outer shell of the hollow sphere, respectively.

Since $\rho(r)$ is a constant, it can be brought forward from the integration:

$$R_g^2 = \frac{\rho(r) \int_{r_1}^{r_2} r^4 dr}{\rho(r) \int_{r_1}^{r_2} r^2 dr} = \frac{\left[\frac{1}{5} r^5\right]_{r_1}^{r_2}}{\left[\frac{1}{3} r^3\right]_{r_1}^{r_2}} = \frac{3({r_2}^5 - {r_1}^5)}{5({r_2}^3 - {r_1}^3)}$$

For a rigid sphere, input $r_2 = b$, $r_1 = 0$. For a hollow sphere, input $r_2 = b$, $r_1 = a$, $(b > a > 0)$:

$$R_{g\,\text{hollow}}^2 - R_{g\,\text{rigid}}^2$$

$$= \frac{3(b^5 - a^5)}{5(b^3 - a^3)} - \frac{3(b^5 - 0^5)}{5(b^3 - 0^3)}$$

$$= \frac{3(b^5 - a^5)}{5(b^3 - a^3)} - \frac{3b^2(b^3 - a^3)}{5(b^3 - a^3)}$$

$$= \frac{3(b^5 - a^5 - b^5 + a^3b^2)}{5(b^3 - a^3)}$$

$$= \frac{3a^3(b^2 - a^2)}{5(b^3 - a^3)} > 0$$

$$\because a^3 > 0, (b^3 - a^3) > 0, \ \ (b^2 - a^2) > 0$$

$$\therefore \ R_{g\,\text{hollow}}^2 > R_{g\,\text{rigid}}^2$$

Table S1. SAXS measurement parameters

(a) Sample details

	gFc	aFc
Organism	*Homo sapiens*	*Homo sapiens*
Source	Papain digestion of human monoclonal IgG1[13]	*Escherichia coli*-expressed[13]
Uniprot sequence ID	P01857	P01857
Molar extinction coefficient (A_{280}, $M^{-1}cm^{-1}$)	71,570	71,570
Partial specific volume (v, $cm^3\ g^{-1}$)	0.7425[6]	0.7425[6]
Average excess scattering density ($10^{10}\ cm^{-2}$)	2.8[6]	2.8[6]
M from chemical composition (Da)	52,926.9	51,235.6
M from mass spectrometry (Da)	52,917.9	51,296.7

(b) SAXS data collection parameters

Instrument	Beamline BL-10C with Dectris PILATUS 2M detector, the Photon Factory (PF) of the High Energy Acceleration Research Organization (KEK)
Wavelength (Å)	1.2
Beam size (mm^2)	1.1 × 1.3
Camera length (m)	2.028, determined based on a scattering pattern of silver behenate as a standard[14]
q measurement range ($Å^{-1}$)	0.006–0.350
Absolute scaling method	Comparison with scattering from 1.25 mm of pure H_2O
Normalization	To incident beam intensity
Monitoring for radiation damage	Frame-by-frame comparison of data
Exposure time	2 s
Sample configuration	Sample flow system using syringe pump with flow-type cell, sample path length of 1.25 mm
Sample temperature (°C)	25.0 ± 0.1

(c) Software employed for SAXS data reduction, analysis, and interpretation

SAXS data reduction	*Nika*[15]
Extinction coefficient estimate	*ProtParam*[16]
Basic analyses: Guinier, $P(r)$, V_P	*PRIMUSqt* from *ATSAS* 2.8.2[17]
Atomic structure modeling	*CRYSOL*[5] in *ATSAS* 2.8.2
Missing sequence modeling	*MODELLER* 9.16[18, 19]
Three-dimensional graphic model representation	*PyMOL* v.1.6.0.0. Win64,[20] *UCSF Chimera* v.1.11.2.[21]

(d) Structural parameters

	gFc	aFc
Guinier analysis (for low q region)		
$I(0)$ (cm^{-1})	0.039 ± 0.000 (3 mg/mL) 0.038 ± 0.000 (interference-free)	0.036 ± 0.000 (3 mg/mL) 0.036 ± 0.000 (interference-free)
R_g (Å)	27.49 ± 0.19 (3 mg/mL) 26.44 ± 0.31 (interference-free)	28.69 ± 0.19 (3 mg/mL) 28.88 ± 0.31 (interference-free)
q_{min} ($Å^{-1}$)	0.02	0.02
qR_g max	1.23 (3 mg/mL) 1.18 (interference-free)	1.28 (3 mg/mL) 1.29 (interference-free)
Coefficient of correlation, R^2	0.99 (3 mg/mL) 0.96 (interference-free)	0.99 (3 mg/mL) 0.96 (interference-free)
M from $I(0)$ (kDa) (ratio to predicted)	53.7 (1.01) (3 mg/mL) 53.3 (1.01) (interference-free)	50.6 (0.99) (3 mg/mL) 50.7 (0.99) (interference-free)
Kratky analysis		
$q_{m,small}$ ($Å^{-1}$)	0.064 (3 mg/mL)	0.062 (3 mg/mL)
$q^2I(q_{m,small})$ (10^{-5} cm^{-1})	5.87 (3 mg/mL)	4.96 (3 mg/mL)
$I(0)$ (cm^{-1})	0.039 (3 mg/mL)	0.035 (3 mg/mL)
R_g (Å)	27.07 (3 mg/mL)	27.77 (3 mg/mL)
$P(r)$ analysis by GNOM[11]		

R_g (Å)	27.87 (3 mg/mL) 27.60 (interference-free)	28.50 (3 mg/mL) 28.32 (inter-ference free)
D_{max} (Å)	102 (3 mg/mL) 97 (interference-free)	98 (3 mg/mL) 102 (interference-free)
q range (Å^{-1})	0.019–0.296 (3 mg/mL) 0.019–0.309 (interference-free)	0.019–0.350 (3 mg/mL) 0.019–0.330 (interference-free)
Total estimate from GNOM	0.61 (3 mg/mL) 0.80 (interference-free)	0.87 (3 mg/mL) 0.76 (interference-free)
Porod volume (Å^3) (ratio V_p/calculated M)	66,600 (1.26) (3 mg/mL) 65,300 (1.23) (interference-free)	59,800 (1.17) (3 mg/mL) 60,600 (1.18) (interference-free)

Table S2. Information on the Fc crystal structures used in the current study

PDBID		First right singular vector	Chi^2 value, gFc	*P*-value, gFc	Chi^2 value, aFc	*P*-value, aFc	Complex	Reference
1FC1		-0.003	0.059	0.000	0.088	0.000	–	22
1H3U		-0.063	0.022	0.000	0.035	0.005	–	23
1H3V		-0.030	–	–	–	–	–	23
1H3X		-0.061	0.025	0.000	0.041	0.001	–	23
1H3Y		-0.082	–	–	–	–	–	23
1HZH		-0.087	0.020	0.020	0.026	0.010	–	24
2DTS		-0.106	0.019	0.153	0.029	0.492	–	25
2WAH		0.294	0.403	0.000	0.392	0.000	–	26
3AVE		-0.101	0.021	0.010	0.031	0.005	–	25
3DO3	gFc	-0.097	0.031	0.000	0.044	0.001	–	–
3V95		-0.099	0.021	0.000	0.034	0.001	–	27
4BYH		-0.100	0.068	0.000	0.080	0.000	–	28
4CDH		-0.060	0.039	0.000	0.055	0.000	–	29
4KU1		-0.037	0.105	0.000	0.128	0.000	–	30
4Q7D		-0.052	0.021	0.000	0.031	0.005	–	31
4W4N		-0.045	0.021	0.000	0.032	0.005	–	32
4WI2		-0.108	0.024	0.000	0.035	0.005	–	–
5GSQ		-0.341	0.023	0.000	0.031	0.079	–	33
5JII		0.300	0.533	0.000	0.513	0.000	–	–
1E4K		0.207	0.182	0.000	0.210	0.000	FcγRIII	34
1T83	gFc + FcγR	0.070	0.126	0.000	0.120	0.000	FcγRIII-b	35
1T89		0.073	0.190	0.000	0.218	0.000	FcγRIII-b	35

3AY4		0.083	0.104	0.000	0.116	0.000	FcγRIII-a	36
3RY6		0.149	0.151	0.000	0.169	0.000	FcγRII-a	37
3SGJ		0.163	0.161	0.000	0.182	0.000	FcγRIII-a	38
3SGK		0.148	0.197	0.000	0.219	0.000	FcγRIII-a	38
4W4O		0.131	0.135	0.000	0.149	0.000	FcγRI	32
4X4M		0.141	0.224	0.000	0.227	0.000	FcγRI	39
4ZNE		0.123	0.146	0.000	0.160	0.000	FcγRI	40
1DN2	gFc + binding protein	0.174	0.231	0.000	0.225	0.000	Engineered peptide	41
1FCC		0.126	0.145	0.000	0.171	0.000	Streptococcal protein G (C2 fragment)	42
1OQO		-0.097	0.023	0.001	0.032	0.005	–	–
1OQX		-0.119	0.019	0.040	0.027	0.079	–	–
2GJ7		0.174	0.229	0.000	0.236	0.000	Glycoprotein E	43
2IWG		0.288	0.564	0.000	0.542	0.000	52-kDa RO protein	44
2J6E		-0.170	0.026	0.000	0.030	0.153	IgM	45
3D6G		-0.102	0.024	0.000	0.036	0.001	Protein-A mimetic peptide dendrimer ligand	–
3WKN		-0.103	0.027	0.000	0.042	0.001	AFFinger p17	46
5U4Y		-0.069	0.021	0.020	0.028	0.010	Protein A	47
5U52		-0.171	0.019	0.492	0.027	0.079	Mini Z domain	47
3DNK	aFc	0.058	0.097	0.000	0.102	0.000	–	–
3S7G		-0.399	0.056	0.000	0.056	0.000	–	–

SUPPLEMENTARY FIGURE LEGENDS

Figure S1.

Concentration dependence and normalization of SAXS profiles for gFc (a, b, e, f) and aFc (c, d, g, h). SAXS profiles of each sample at 2–5 mg/mL in a log-log plot (a–d) and Guinier plots in the low q region (e–h). Concentration-normalized SAXS profiles in a log-log plot (b, d) and Guinier plots in the low q region (f, h). The black line in Guinier plots represents the fitted region of the Guinier approximation. The results of the Guinier approximation of each concentration are also shown, $I(0)$ (i) and R_g (j); The black line represents the regression line of the concentration dependence of $R(g)$ and $I(0)$.

Figure S2.

Interference-free SAXS profiles. The log-linear plot (a), Kratky plot (b), and Guinier plot (c). The black straight line indicates the fitted region of the Guinier approximation. The pair-distance distribution function calculated by the indirect Fourier transformation (d). The solid and dotted lines indicate pair-distance distribution function of the interference-free SAXS profiles and 3 mg/mL SAXS profiles, respectively.

Figure S3.

Characteristics of the left and right singular vectors of the first to seventh principal components. (Left) Porcupine plots of each left singular vector. The yellow line indicates the averaged three-dimensional coordinates of Cα atoms calculated from the crystal structure dataset. The green spine indicates the direction and magnitude of the deviation of each left singular vector from the averaged three-dimensional coordinate of Cα atoms. (Right) The right singular vector of each crystal structure.

Figure S4.

Random-like distribution of the reduced chi-square values for the 3 mg/mL SAXS profiles. The reduced chi-square value of 100 intact model structures for each of the 40 template structures of gFc (a) and aFc (b). (c, d) The reduced chi-square distribution of 1HZH (red), 1OQX (blue), 2DTS (green), 5U4Y (orange), and 5U52 (purple), which exhibited the lowest median chi-square values among the 40 template structures.

Figure S5.

(a) A correlation plot of reduced chi-square values for the interference-free SAXS profiles of gFc and aFc. The inset contains the plot of the lowest reduced chi-square value. For calculation of the reduced chi-square value, the experimental errors at each q of the 3 mg/mL SAXS profiles were used as those

of the interference-free SAXS profiles. (b, c) Correlation plots between the reduced chi-square values for 3 mg/mL SAXS profile and the interference-free SAXS profiles.

Figure S6.

Correlation between the reduced chi-square value for 3 mg/mL SAXS profiles and the first to seventh right singular vectors (V*i*, *i* = 1–7).

Figure S7.

Correlation plots between the chi-square value for 3 mg/mL SAXS profiles and the first right singular. The values of the four model structures proposed by Remesh et al. were plotted with the 40 model structures of gFc used in the current study.

Figure S8.

Mass spectra of gFc (a) and aFc (b). Molecular masses of each peak and glycoform assigned based on the mass difference between the peaks are shown.

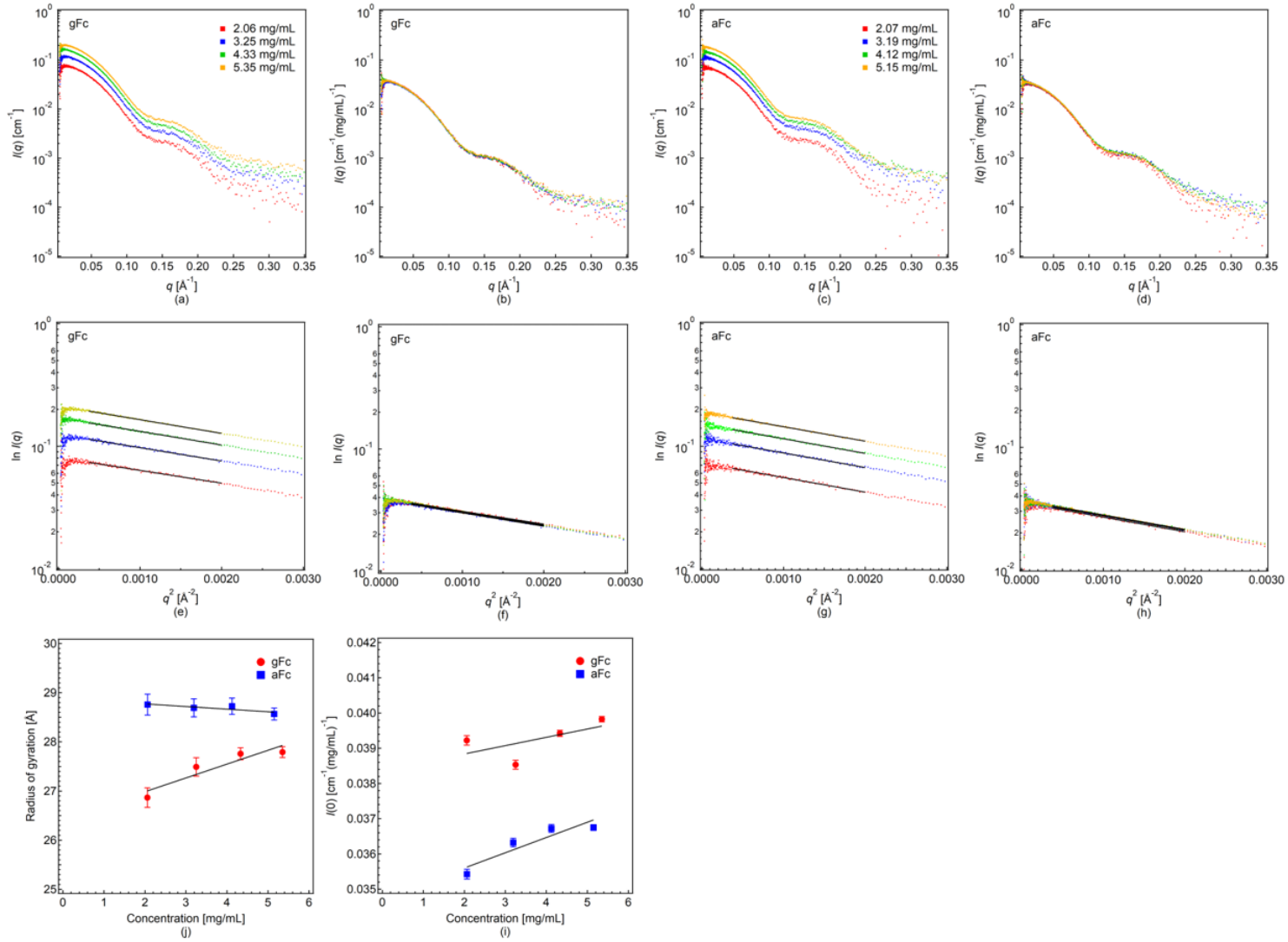
gFc
2.06 mg/mL
3.25 mg/mL
4.33 mg/mL
5.35 mg/mL
I(q) [cm-1]
q [Å-1]
(a)
gFc
I(q) [cm-1 (mg/mL)-1]
q [Å-1]
(b)
aFc
2.07 mg/mL
3.19 mg/mL
4.12 mg/mL
5.15 mg/mL
I(q) [cm-1]
q [Å-1]
(c)
aFc
I(q) [cm-1 (mg/mL)-1]
q [Å-1]
(d)
gFc
ln I(q)
q2 [Å-2]
(e)
gFc
ln I(q)
q2 [Å-2]
(f)
aFc
ln I(q)
q2 [Å-2]
(g)
aFc
ln I(q)
q2 [Å-2]
(h)
gFc
aFc
Radius of gyration [Å]
Concentration [mg/mL]
(j)
gFc
aFc
I(0) [cm-1 (mg/mL)-1]
Concentration [mg/mL]
(i)

Figure S1

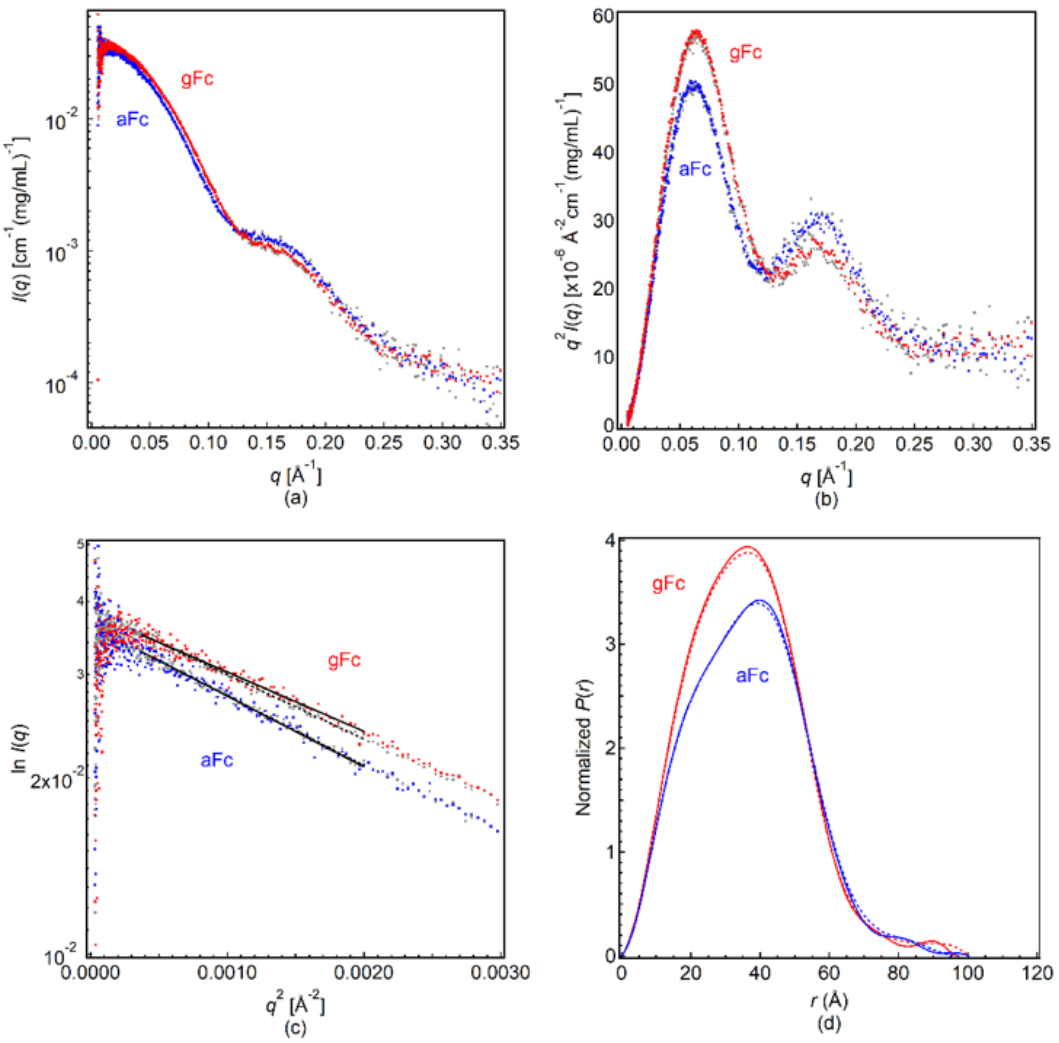
gFc
aFc
I(q) [cm-1 (mg/mL)-1]
q [Å-1]
(a)
gFc
aFc
q2 I(q) [x10-6 Å-2cm-1 (mg/mL)-1]
q [Å-1]
(b)
gFc
aFc
ln I(q)
q2 [Å-2]
(c)
gFc
aFc
Normalized P(r)
r (Å)
(d)

Figure S2

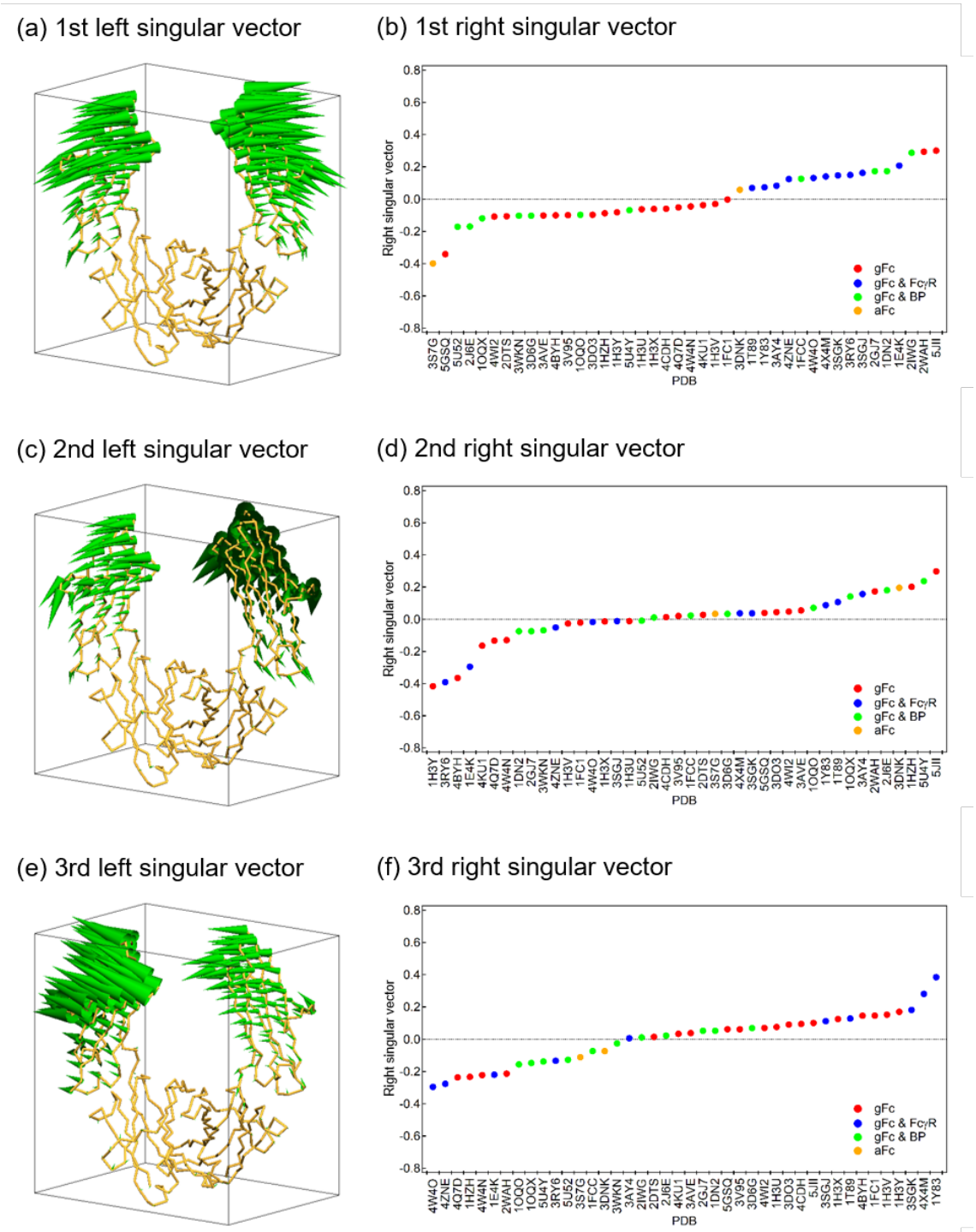
(a) 1st left singular vector
(b) 1st right singular vector
Right singular vector
PDB
gFc
gFc & FcγR
gFc & BP
aFc
(c) 2nd left singular vector
(d) 2nd right singular vector
Right singular vector
PDB
gFc
gFc & FcγR
gFc & BP
aFc
(e) 3rd left singular vector
(f) 3rd right singular vector
Right singular vector
PDB
gFc
gFc & FcγR
gFc & BP
aFc

Figure S3

(g) 4th left singular vector

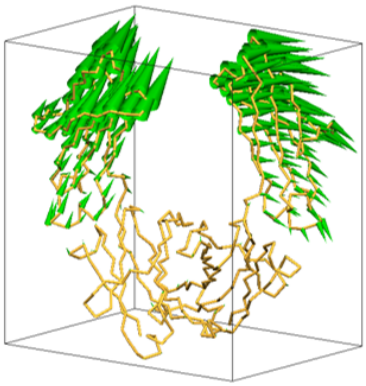

(h) 4th right singular vector

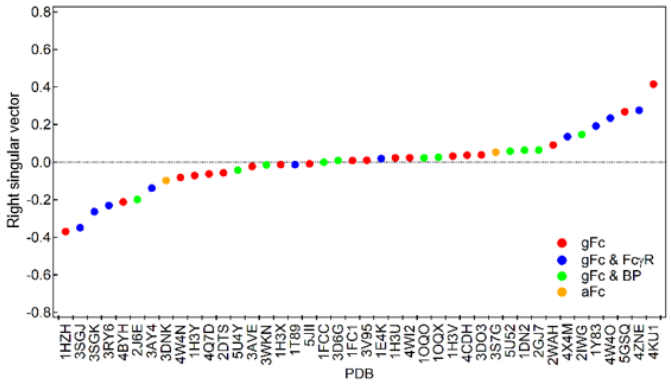

(i) 5th left singular vector

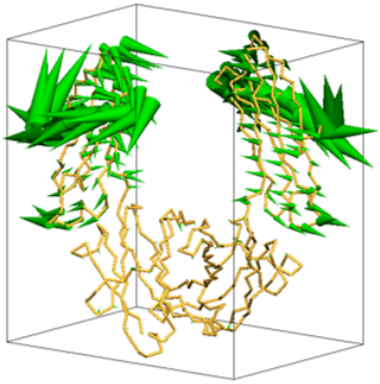

(j) 5th right singular vector

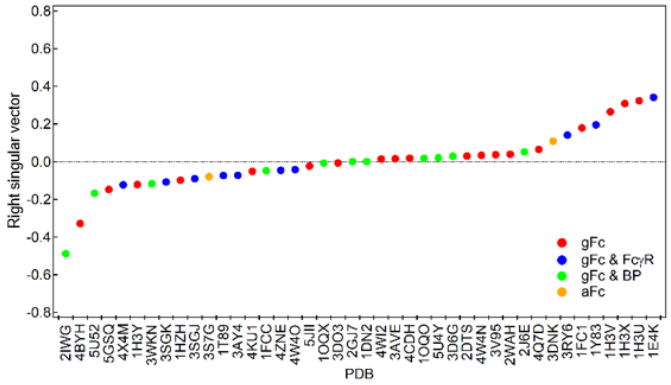

(k) 6th left singular vector

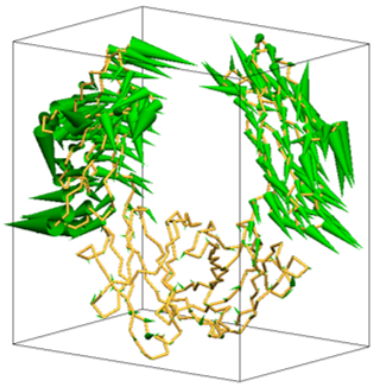

(l) 6th right singular vector

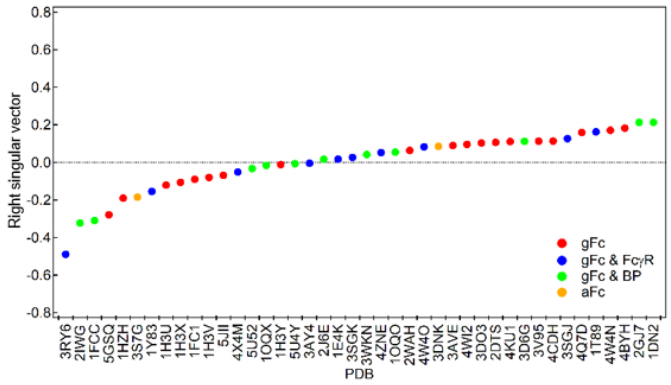

Figure S3 (continued)

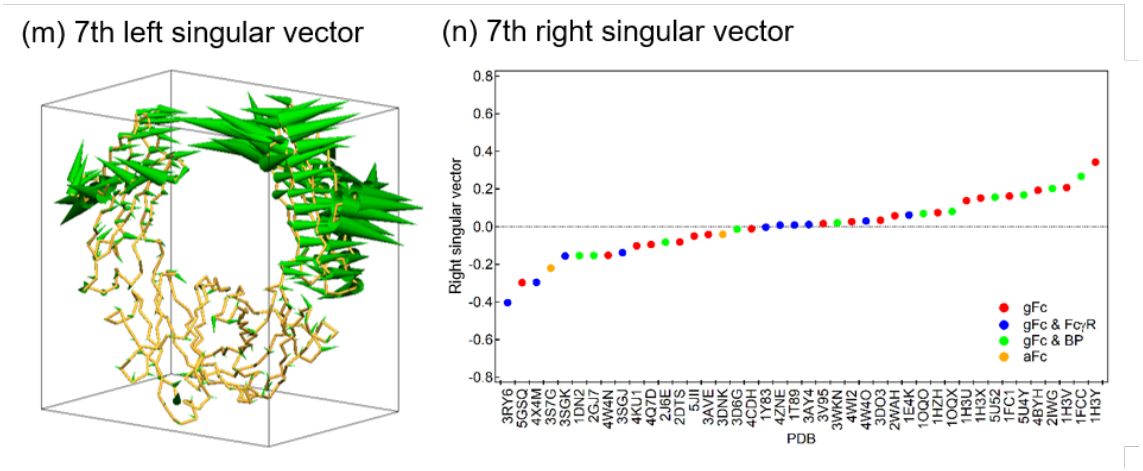

Figure S3 (continued)

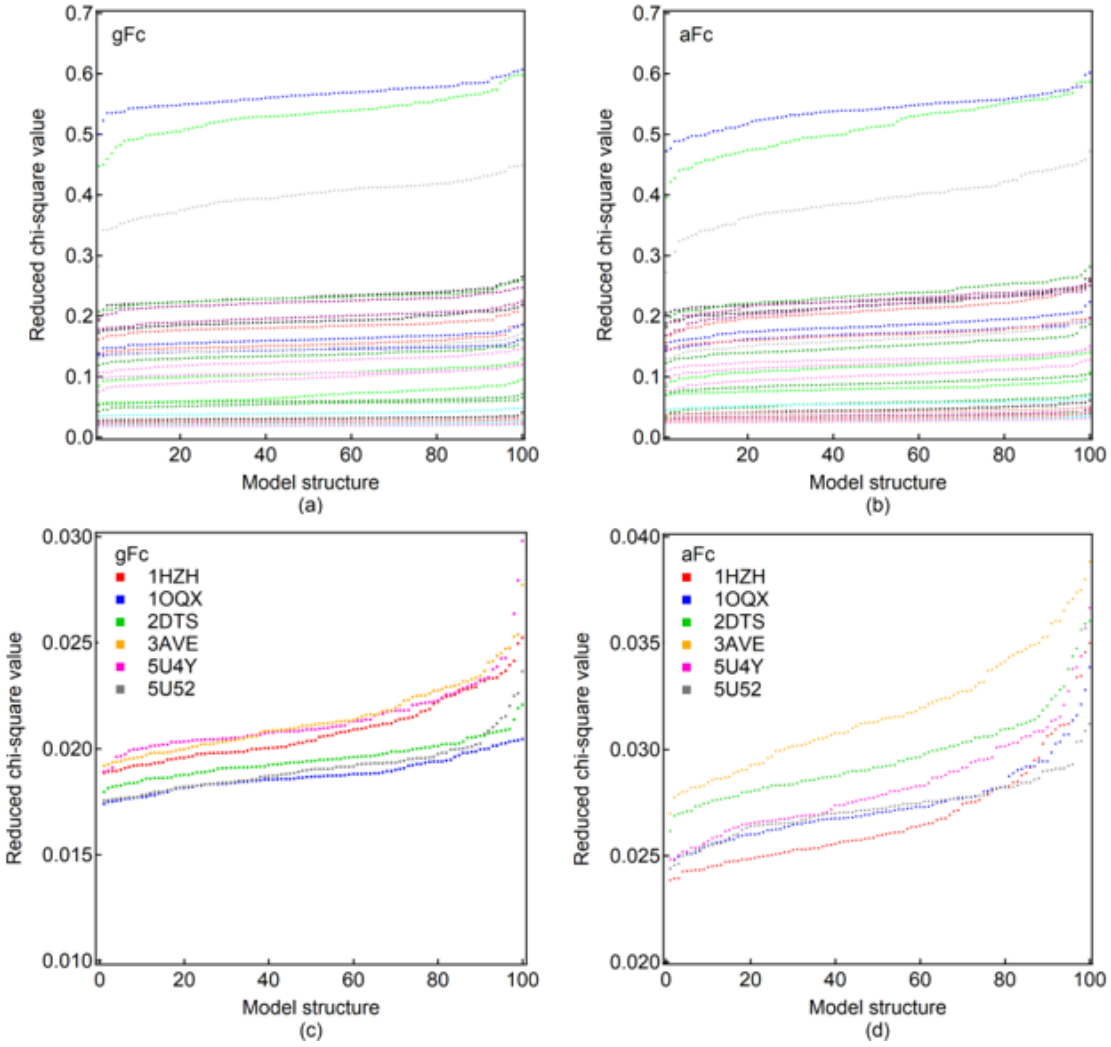
gFc
Reduced chi-square value
Model structure
(a)
aFc
Reduced chi-square value
Model structure
(b)
gFc
1HZH
1OQX
2DTS
3AVE
5U4Y
5U52
Reduced chi-square value
Model structure
(c)
aFc
1HZH
1OQX
2DTS
3AVE
5U4Y
5U52
Reduced chi-square value
Model structure
(d)

Figure S4

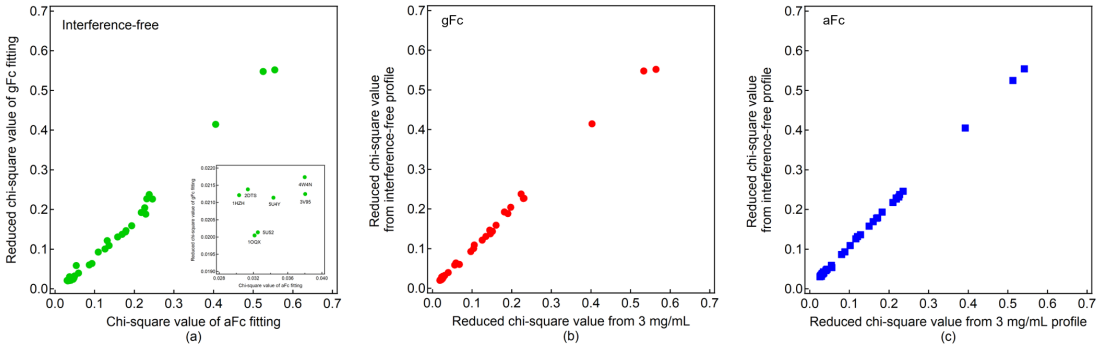
Interference-free
Reduced chi-square value of gFc fitting
Chi-square value of aFc fitting
(a)
gFc
Reduced chi-square value from interference-free profile
Reduced chi-square value from 3 mg/mL
(b)
aFc
Reduced chi-square value from interference-free profile
Reduced chi-square value from 3 mg/mL profile
(c)

Figure S5

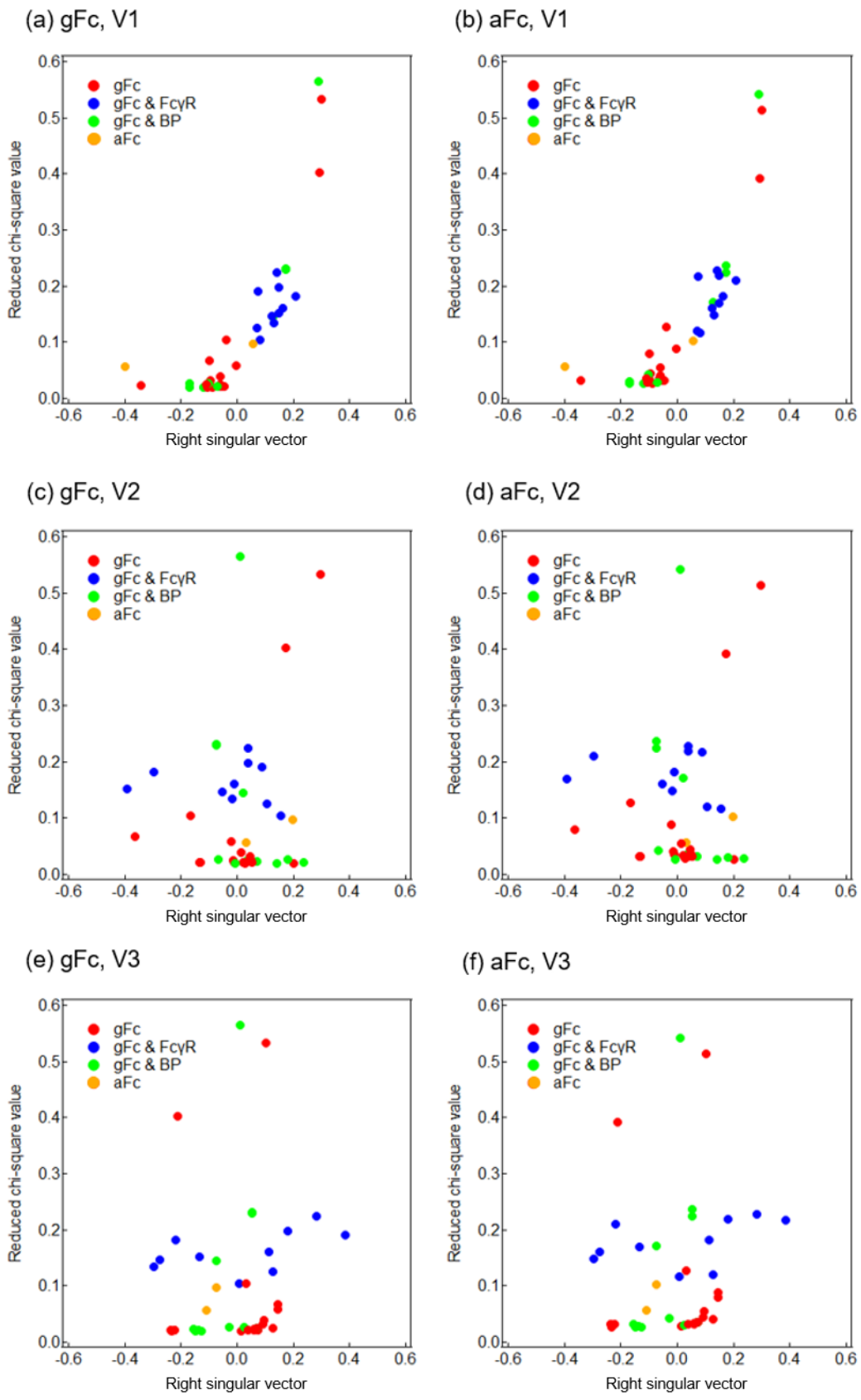
(a) gFc, V1
(b) aFc, V1
(c) gFc, V2
(d) aFc, V2
(e) gFc, V3
(f) aFc, V3
gFc
gFc & FcγR
gFc & BP
aFc
Reduced chi-square value
Right singular vector
0.0
0.1
0.2
0.3
0.4
0.5
0.6
-0.6
-0.4
-0.2
0.0
0.2
0.4
0.6

Figure S6

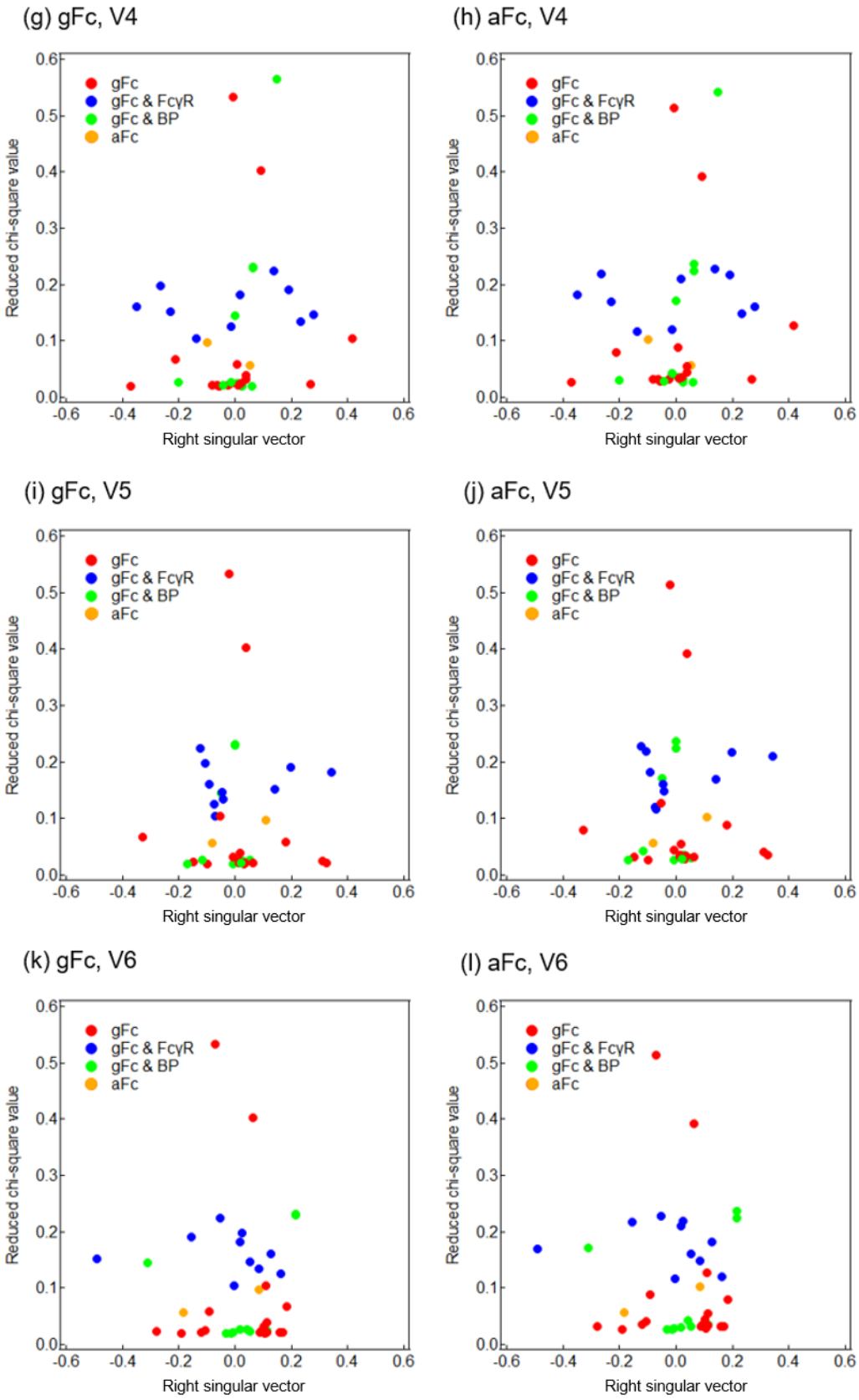

Figure S6 (continued)

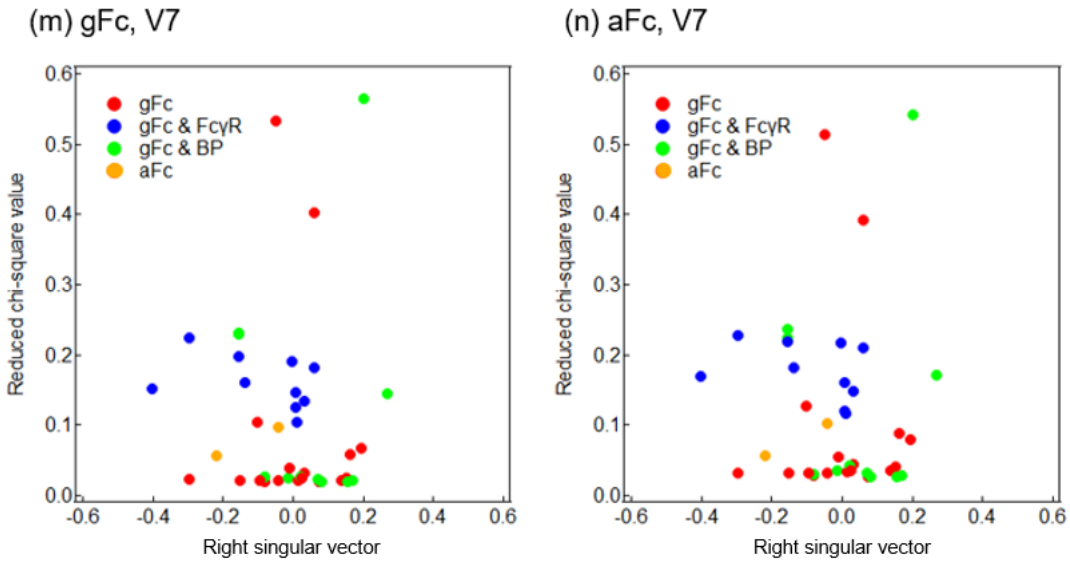

Figure S6 (continued)

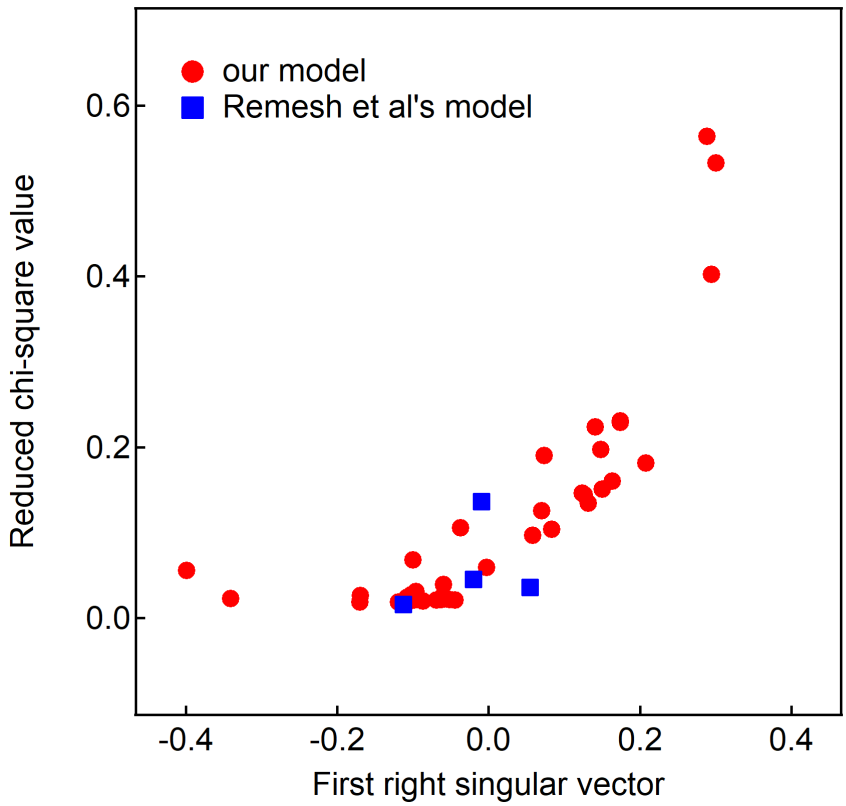
our model
Remesh et al's model
Reduced chi-square value
0.6
0.4
0.2
0.0
-0.4
-0.2
0.0
0.2
0.4
First right singular vector

Figure S7

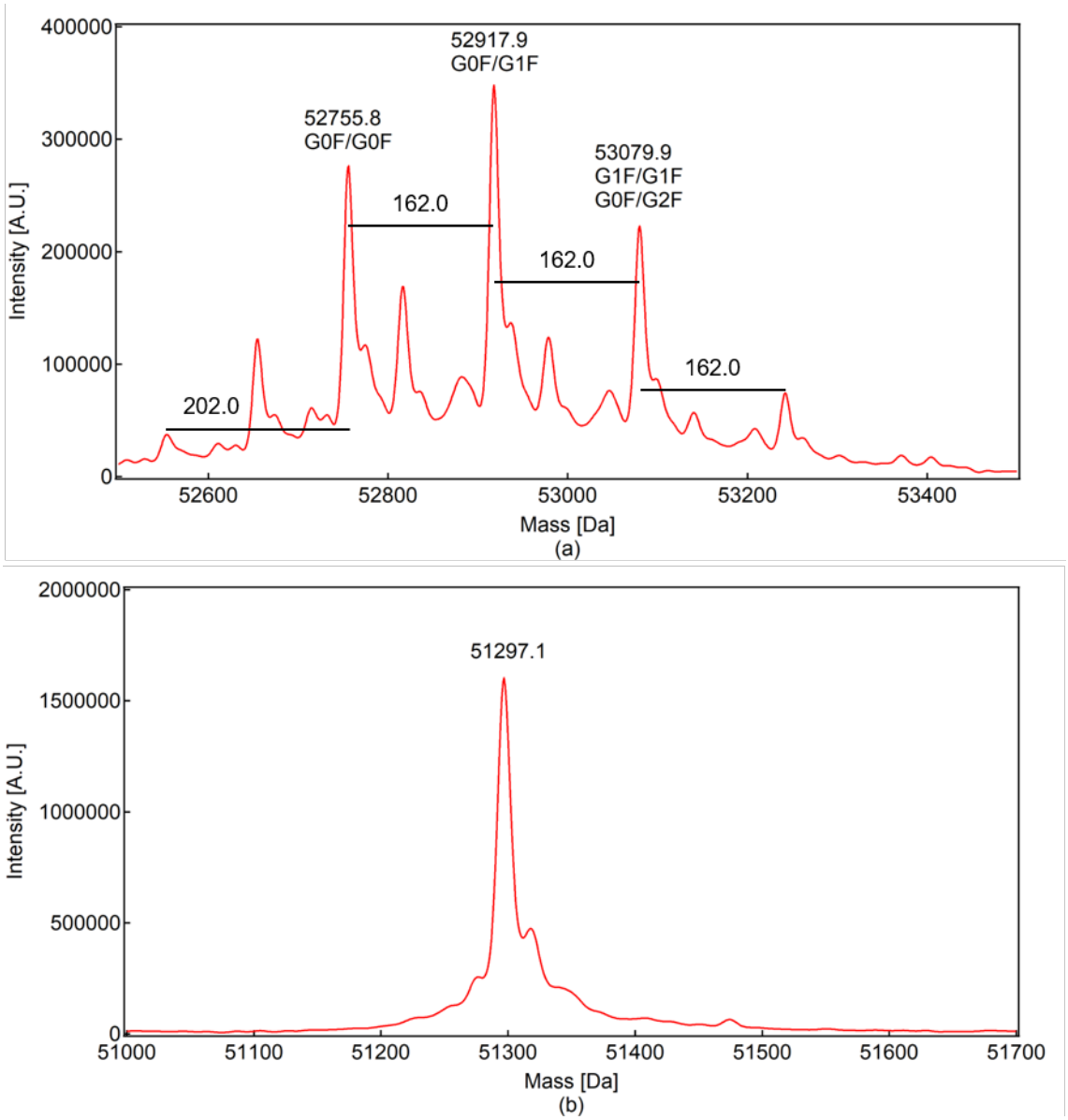
400000
300000
200000
100000
0
Intensity [A.U.]
52917.9
G0F/G1F
52755.8
G0F/G0F
53079.9
G1F/G1F
G0F/G2F
162.0
162.0
162.0
202.0
52600
52800
53000
53200
53400
Mass [Da]
(a)
2000000
1500000
1000000
500000
0
Intensity [A.U.]
51297.1
51000
51100
51200
51300
51400
51500
51600
51700
Mass [Da]
(b)

Figure S8

REFERENCES

1. Morimoto M, Imamura H, Shibuta S, Morita T, Nishikawa K, Yamamoto H, et al. Asphaltene Aggregation Behavior in Bromobenzene Determined By Small-angle X-ray Scattering. Energy & Fuels. 2015;29(9):5737–43. doi: 10.1021/acs.energyfuels.5b01491.
2. Orthaber D, Bergmann A, Glatter O. SAXS experiments on absolute scale with Kratky systems using water as a secondary standard. Journal of Applied Crystallography. 2000;33:218–25. doi: 10.1107/S0021889899015216.
3. Svergun DI, Koch MHJ, Timmins PA, May RP. Small Angle X-Ray and Neutron Scattering from Solutions of Biological Macromolecules. United States of America: Oxford University Press; 2013.
4. Daniel F, Alexey G K , Dmitri I S. Automated acquisition and analysis of small angle X-ray scattering data. 2012;689:52–59. Doi: 10.1016/j.nima.2012.06.008.
5. Svergun D, Barberato C, Koch M. CRYSOL - A program to evaluate x-ray solution scattering of biological macromolecules from atomic coordinates. Journal of Applied Crystallography. 1995;28:768-73. doi: 10.1107/S0021889895007047.
6. Mylonas E, Svergun D. Accuracy of molecular mass determination of proteins in solution by small-angle X-ray scattering. Journal of Applied Crystallography. 2007;40:S245–S9. doi: 10.1107/S002188980700252X.
7. Morita T, Kurihara K, Yoshida O, Imamura H, Hatakeyama Y, Nishikawa K, et al. Fusion Growth of Gold Nanoparticles Induced by the Conformational Change of a Thermoresponsive Polymer Studied by Distance Distribution Functions. Journal of Physical Chemistry C. 2013;117(26):13602–8. doi: 10.1021/jp310906b.
8. Fukuyama K, Kasahara Y, Kasahara N, Oya A, Nishikawa K. Small-angle X-ray scattering study of the pore structure of carbon fibers prepared from a polymer blend of phenolic resin and polystyrene. Carbon. 2001;39(2):287–90. doi: 10.1016/S0008-6223(00)00159-7.
9. Glatter O, Kratky O. Small Angle X-ray Scattering. London: Academic Press; 1982.
10. Waser J, Schomaker V. The Fourier Inversion of Diffraction Data. Reviews of Modern Physics. 1953;25(3):671–90. doi: 10.1103/RevModPhys.25.671.
11. Svergun D. Determination of the Regularization Parameter in Indirect-Transform Methods Using Perceptual Criteria. Journal of Applied Crystallography. 1992;25:495–503. doi: 10.1107/S0021889892001663.
12. Feigin LA, Svergun DI, Taylor GW. Structure Analysis by Small-Angle X-Ray and Neutron Scattering. United States of America: Springer; 1987.
13. Yageta S, Shibuya R, Imamura H, Honda S. Conformational and Colloidal Stabilities of Human Immunoglobulin G Fc and Its Cyclized Variant: Independent and Compensatory Participation of Domains in Aggregation of Multidomain Proteins. Mol Pharm. 2017;14(3):699–711 doi:

10.1021/acs.molpharmaceut.6b00983.

14. Huang T, Toraya H, Blanton T, Wu Y. X-ray Powder Diffraction Analysis of Silver Behenate, a Possible Low-Angle Diffraction Standard. Journal of Applied Crystallography. 1993;26:180–4. doi: 10.1107/S0021889892009762.
15. Ilavsky J. Nika: software for two-dimensional data reduction. Journal of Applied Crystallography. 2012;45:324–8. doi: 10.1107/S0021889812004037.
16. Wilkins MR, Gasteiger E, Bairoch A, Sanchez JC, Williams KL, Appel RD, et al. Protein identification and analysis tools in the ExPASy server. Methods Mol Biol. 1999;112:531–52. doi: 10.1385/1-59259-890-0:571
17. Konarev P, Volkov V, Sokolova A, Koch M, Svergun D. PRIMUS: a Windows PC-based system for small-angle scattering data analysis. Journal of Applied Crystallography. 2003;36:1277–82. doi: 10.1107/S0021889803012779.
18. Webb B, Sali A. Comparative Protein Structure Modeling Using MODELLER. Curr Protoc Bioinformatics. 2014;47:5.6.1–32. doi: 10.1002/0471250953.bi0506s47.
19. Webb B, Sali A. Protein Structure Modeling with MODELLER. Methods Mol Biol. 2017;1654:39–54. doi: 10.1007/978-1-4939-7231-9_4.
20. Schrödinger L. The PyMOL Molecular Graphics System, Version 1.6.0.0.
21. Pettersen E, Goddard T, Huang C, Couch G, Greenblatt D, Meng E, et al. UCSF chimera - A visualization system for exploratory research and analysis. Journal of Computational Chemistry. 2004;25(13):1605–12. doi: 10.1002/jcc.20084.
22. Deisenhofer J. Crystallographic refinement and atomic models of a human Fc fragment and its complex with fragment B of protein A from Staphylococcus aureus at 2.9- and 2.8-A resolution. Biochemistry. 1981;20(9):2361–70. doi: 10.1021/bi00512a001
23. Krapp S, Mimura Y, Jefferis R, Huber R, Sondermann P. Structural analysis of human IgG-Fc glycoforms reveals a correlation between glycosylation and structural integrity. J Mol Biol. 2003;325(5):979–89. doi: 10.1016/S0022-2836(02)01250-0
24. Saphire EO, Parren PW, Pantophlet R, Zwick MB, Morris GM, Rudd PM, et al. Crystal structure of a neutralizing human IGG against HIV-1: a template for vaccine design. Science. 2001;293(5532):1155–9. doi: 10.1126/science.1061692.
25. Matsumiya S, Yamaguchi Y, Saito J, Nagano M, Sasakawa H, Otaki S, et al. Structural comparison of fucosylated and nonfucosylated Fc fragments of human immunoglobulin G1. J Mol Biol. 2007;368(3):767–79. doi: 10.1016/j.jmb.2007.02.034.
26. Crispin M, Bowden TA, Coles CH, Harlos K, Aricescu AR, Harvey DJ, et al. Carbohydrate and domain architecture of an immature antibody glycoform exhibiting enhanced effector functions. J Mol Biol. 2009;387(5):1061–6. doi: 10.1016/j.jmb.2009.02.033.
27. Sibéril S, Ménez R, Jorieux S, de Romeuf C, Bourel D, Fridman WH, et al. Effect of zinc on

human IgG1 and its FcγR interactions. Immunol Lett. 2012;143(1):60–9. doi: 10.1016/j.imlet.2012.02.002

28. Crispin M, Yu X, Bowden TA. Crystal structure of sialylated IgG Fc: implications for the mechanism of intravenous immunoglobulin therapy. Proc Natl Acad Sci U S A. 2013;110(38):E3544–6. doi: 10.1073/pnas.1310657110.
29. Silva-Martín N, Bartual SG, Ramírez-Aportela E, Chacón P, Park CG, Hermoso JA. Structural basis for selective recognition of endogenous and microbial polysaccharides by macrophage receptor SIGN-R1. Structure. 2014;22(11):1595–606. doi: 10.1016/j.str.2014.09.001.
30. Frank M, Walker RC, Lanzilotta WN, Prestegard JH, Barb AW. Immunoglobulin G1 Fc domain motions: implications for Fc engineering. J Mol Biol. 2014;426(8):1799–811. doi: 10.1016/j.jmb.2014.01.011.
31. Ahmed AA, Giddens J, Pincetic A, Lomino JV, Ravetch JV, Wang LX, et al. Structural characterization of anti-inflammatory immunoglobulin G Fc proteins. J Mol Biol. 2014;426(18):3166–79. doi: 10.1016/j.jmb.2014.07.006.
32. Kiyoshi M, Caaveiro JM, Kawai T, Tashiro S, Ide T, Asaoka Y, et al. Structural basis for binding of human IgG1 to its high-affinity human receptor FcγRI. Nat Commun. 2015;6:6866. doi: 10.1038/ncomms7866.
33. Chen CL, Hsu JC, Lin CW, Wang CH, Tsai MH, Wu CY, et al. Crystal Structure of a Homogeneous IgG-Fc Glycoform with the N-Glycan Designed to Maximize the Antibody Dependent Cellular Cytotoxicity. ACS Chem Biol. 2017;12(5):1335–45. doi: 10.1021/acschembio.7b00140.
34. Sondermann P, Huber R, Oosthuizen V, Jacob U. The 3.2-A crystal structure of the human IgG1 Fc fragment-Fc gammaRIII complex. Nature. 2000;406(6793):267–73. doi: 10.1038/35018508.
35. Radaev S, Motyka S, Fridman WH, Sautes-Fridman C, Sun PD. The structure of a human type III Fcgamma receptor in complex with Fc. J Biol Chem. 2001;276(19):16469–77. doi: 10.1074/jbc.M100350200.
36. Mizushima T, Yagi H, Takemoto E, Shibata-Koyama M, Isoda Y, Iida S, et al. Structural basis for improved efficacy of therapeutic antibodies on defucosylation of their Fc glycans. Genes Cells. 2011;16(11):1071–80. doi: 10.1111/j.1365-2443.2011.01552.x.
37. Ramsland PA, Farrugia W, Bradford TM, Sardjono CT, Esparon S, Trist HM, et al. Structural basis for Fc gammaRIIa recognition of human IgG and formation of inflammatory signaling complexes. J Immunol. 2011;187(6):3208–17. doi: 10.4049/jimmunol.1101467.
38. Ferrara C, Grau S, Jäger C, Sondermann P, Brünker P, Waldhauer I, et al. Unique carbohydrate-carbohydrate interactions are required for high affinity binding between FcgammaRIII and antibodies lacking core fucose. Proc Natl Acad Sci U S A. 2011;108(31):12669–74. doi: 10.1073/pnas.1108455108.

39. Lu J, Chu J, Zou Z, Hamacher NB, Rixon MW, Sun PD. Structure of FcγRI in complex with Fc reveals the importance of glycan recognition for high-affinity IgG binding. Proc Natl Acad Sci U S A. 2015;112(3):833–8. doi: 10.1073/pnas.1418812112.
40. Oganesyan V, Mazor Y, Yang C, Cook KE, Woods RM, Ferguson A, et al. Structural insights into the interaction of human IgG1 with FcγRI: no direct role of glycans in binding. Acta Crystallogr D Biol Crystallogr. 2015;71(Pt 11):2354–61. doi: 10.1107/S1399004715018015.
41. DeLano WL, Ultsch MH, de Vos AM, Wells JA. Convergent solutions to binding at a protein-protein interface. Science. 2000;287(5456):1279–83. doi: 10.1126/science.287.5456.1279
42. Sauer-Eriksson AE, Kleywegt GJ, Uhlén M, Jones TA. Crystal structure of the C2 fragment of streptococcal protein G in complex with the Fc domain of human IgG. Structure. 1995;3(3):265–78. doi: 10.1016/S0969-2126(01)00157-5
43. Sprague ER, Wang C, Baker D, Bjorkman PJ. Crystal structure of the HSV-1 Fc receptor bound to Fc reveals a mechanism for antibody bipolar bridging. PLoS Biol. 2006;4(6):e148. doi: 10.1371/journal.pbio.0040148.
44. James LC, Keeble AH, Khan Z, Rhodes DA, Trowsdale J. Structural basis for PRYSPRY-mediated tripartite motif (TRIM) protein function. Proc Natl Acad Sci U S A. 2007;104(15):6200–5. doi: 10.1073/pnas.0609174104.
45. Duquerroy S, Stura EA, Bressanelli S, Fabiane SM, Vaney MC, Beale D, et al. Crystal structure of a human autoimmune complex between IgM rheumatoid factor RF61 and IgG1 Fc reveals a novel epitope and evidence for affinity maturation. J Mol Biol. 2007;368(5):1321–31. doi: 10.1016/j.jmb.2007.02.085.
46. Watanabe H, Honda S. Adaptive Assembly: Maximizing the Potential of a Given Functional Peptide with a Tailor-Made Protein Scaffold. Chem Biol. 2015;22(9):1165–73. doi: 10.1016/j.chembiol.2015.07.015.
47. Ultsch M, Braisted A, Maun HR, Eigenbrot C. 3-2-1: Structural insights from stepwise shrinkage of a three-helix Fc-binding domain to a single helix. Protein Eng Des Sel. 2017;30(9):619–25. doi: 10.1093/protein/gzx029.